Journal of Zhejiang University-SCIENCE C (Computers & Electronics)
ISSN 1869-1951 (Print); ISSN 1869-196X (Online)
www.zju.edu.cn/jzus; www.springerlink.com
E-mail: jzus@zju.edu.cn

An efficient projection defocus algorithm based on multi-scale convolution kernel templates*

Bo ZHU[†1,2], Li-jun XIE[†‡1,2], Guang-hua SONG[1,2], Yao ZHENG[1,2]

([1]*School of Aeronautics and Astronautics, Zhejiang University, Hangzhou 310027, China*)

([2]*Center for Engineering and Scientific Computation, Zhejiang University, Hangzhou 310027, China*)

[†]E-mail: {zhubo, zdxlj}@zju.edu.cn

Received Apr. 3, 2013; Revision accepted Aug. 1, 2013; Crosschecked Sept. 16, 2013

Abstract: The focal problems of projection include out-of-focus projection images from the projector caused by incomplete mechanical focus and screen-door effects produced by projection pixilation. To eliminate these defects and enhance the imaging quality and clarity of projectors, a novel adaptive projection defocus algorithm is proposed based on multi-scale convolution kernel templates. This algorithm applies the improved Sobel-Tenengrad focus evaluation function to calculate the sharpness degree of intensity equalization and then constructs multi-scale defocus convolution kernels to remap and render the defocus projection image. The resulting projection defocus corrected images can eliminate out-of-focus effects and improve the sharpness of uncorrected images. Experiments show that the algorithm works quickly and robustly and that it not only effectively eliminates visual artifacts and can run on a self-designed smart projection system in real time but also significantly improves the resolution and clarity of the observer's visual perception.

Key words: Projection focal, Sobel-Tenengrad evaluation function, Projector defocus, Multi-scale convolution kernels
doi:10.1631/jzus.C1300080 **Document code:** A **CLC number:** TP391

1 Introduction

A projector provides a large flexible projection image to satisfy different display sizes; as a result, projectors play an important role in the fields of education and research as conventional auxiliary visualization equipment. As projectors become more affordable for the consumer, they have become popular in everyday life for personal entertainment. Although the current digital light processing (DLP) projector has eliminated many of the defects found in the liquid-crystal display (LCD) ones, there are still problems that need to be addressed. These problems primarily involve adaptation to irregular display surfaces and involve solutions such as geometric calibration, color compensation, and focal correction technologies. Researchers have proposed several computer vision algorithms for geometric warping and color compensation, but focal correction problems remain a challenge. Given this background, current research focuses primarily on adaptive defocus algorithms for projection images.

2 Related work

Projection focal problems have two primary causes: the out-of-focus problem in projectors that are not completely mechanically focused and the screen-door effect produced by projection pixilation. Such projection artifacts will disturb the observers' perceptions and degrade picture clarity. In recent years, some progress has been made in related areas. Zhang

‡ Corresponding author

* Project supported by the National Natural Science Foundation of China (Nos. 11272285, 61008048, and 10876036), the Zhejiang Provincial Natural Science Foundation (No. LY12F02026), and the Department of Science and Technology of Zhejiang Province (No. 2009C31112), China

and Nayar (2006) and Grosse *et al*. (2010) modeled the projector's defocus using a linear system to develop a temporal defocus analysis method, in order to recover depth at each camera pixel by estimating the parameters of its projection defocus kernel in the frequency domain. Bimber and Emmerling (2006) and Nagase *et al*. (2011) proposed a solution using multiple conventional projectors with overlapping images, applying motorized adjustments of the lens system and the camera feedback to measure the relative focal value of every projector pixel for different focal planes. Brown *et al*. (2006) applied a preconditioning method to the original image before projection blurring using a camera to estimate a series of spatially varying point-spread functions (PSFs) across the projector's image. The PSFs are then used to guide a preprocessing algorithm based on Wiener filtering, assuming that the display surface is planar and Lambertian. Oyamada and Saito (2009) proposed another novel spatially varying PSF-based method, which covers the entire projection image and is computed by interpolation. By pre-correcting every projected sub-image, this pre-correction method reduces out-of-focus projection blur without projecting the feature image.

In our study, a novel adaptive projection defocus algorithm is proposed based on multi-scale convolution kernel templates. Compared with previous research, this method works faster and is more robust. Our main contributions are listed as follows:

1. The algorithm does not require multiple projectors or auxiliary optical calculation equipment to construct a complex defocus projection system, which makes the projection defocus system much simpler.

2. This method provides a novel focus-evaluation function to obtain a defocus estimation kernel template, in preference to applying the optimization iteration method, which requires considerable computational time for the multiple iteration steps necessary to ensure accurate defocus results. This improvement is very important to satisfy the need for projection defocus in real time.

3. The significant defocus accuracy from applying this multi-scale convolution defocus computation and added radiometric optimization algorithm can effectively eliminate projection blur and enhance the defocus projection effect to adapt to environmental textures and satisfy the observer's visual criterion.

3 Preprocessing of defocus correction

3.1 Calibration of the projector-camera system

The projector-camera system consists of one projector and one camera, which are controlled by a computer running the projector defocus calibration programs. To initialize the system and establish the corresponding mapping between the projector space and the camera space at the pixel level, the projector-camera system requires complete system calibration in advance.

The system initialization primarily involves the camera calibration procedure. We use Zhang (2000)'s camera calibration method to rectify the radial and tangential distortion of a mounted camera using its intrinsic parameters. The calibrated camera can capture the projection display environment and radiometric information in real time.

Several popular calibration algorithms have been used in research on projection geometric correction (Raskar *et al*., 1998; Brown *et al*., 2005; Bhasker *et al*., 2007; Xie *et al*., 2007; Yang *et al*., 2007). In this work, to establish the corresponding mapping from the projector space to the camera space at the pixel level, we propose a binary encoded structured light method combined with a discrete mapping algorithm. According to defocus function model estimation, Gaussian blobs of equal size are rendered as a feature pattern, and used to create binary encoded structured light. The discrete mapping algorithm can then be used to compute the corresponding per-pixel mapping. Details about this process can be found in Zhu *et al.* (2011a).

3.2 Radiometric compensation optimization

For disturbances that come from geometric distortion and radiometric errors, images captured by a projector-camera system without any processing cannot be used directly in projection defocus correction. The method described in Section 3.1 can complete the geometric calibration simply and effectively and, for the second problem, a radiometric compensation algorithm is proposed to optimize geometric corrected projection images.

Certain everyday environments, such as curtains with a regular texture or walls painted a certain color, can also be used as projection display surfaces, but the material, decorative pattern, and even natural light

will disturb the radiometry and intensity of the initial projection image. Several recent studies (Nayar *et al*., 2003; Grossberg *et al*., 2004; Ashdown *et al*., 2006; Wang *et al*., 2007; Bimber *et al*., 2008) focused on this problem. In this study, the radiometric compensation algorithm based on the improved Lambertian reflection model (Zhu *et al*., 2011a; 2011b; 2012) is used to correct the radiometry and the intensity of the projection image.

The Lambertian reflection model is an ideal estimation for a non-smooth reflection surface. In this model, it is assumed that the radiometry and intensity can be reflected completely and equally. The parameterization model depends on three key factors: incident light, R_I; the unit vector from incident light, $\boldsymbol{i}$; and the normal vector to the reflection surface, $\boldsymbol{n}$. α is the angle between vectors $\boldsymbol{i}$ and $\boldsymbol{n}$. The standard Lambertian radiometric reflection can be parameterized as

$$R_S = (\boldsymbol{i}\cdot\boldsymbol{n})\cdot R_I = \|\boldsymbol{i}\|\cdot\|\boldsymbol{n}\|\cdot\cos\alpha\cdot R_I = R_I\cdot\cos\alpha. \quad (1)$$

To improve the standard Lambertian reflection model, two parameters T and R_E are added to describe the material texture and environmental light, obtained by an environment radiometric reconstruction method. Details of the environment radiometric reconstruction method can be found in Zhu *et al*. (2011a; 2011b; 2012). The incident radiometric light can thus be computed as follows:

$$R_I = \frac{R - R_E\cdot T}{T\cdot\cos\alpha}. \quad (2)$$

In projection display environments, R_I is a projection beam from the projector light source, and the surface radiometric reflection R can be calculated by extracting the red, green, and blue components from a captured RGB image. As a result of a previous analysis, the improved Lambertian reflection model is constructed to calculate the radiometric compensation data. In Eq. (2), substitute R with the original projection image, $I_{(R, G, B)}$, to obtain the ideal compensation projection data C (red, green, and blue components are calculated separately). Applying the ideal compensation projection data C to the initial projection defocus image, the final radiometric compensated projection defocus image is obtained (in the ideal case, α can be set as 0 and thus $\cos\alpha$=1 for experiments):

$$C = \frac{I - R_E\cdot T}{T\cdot\cos\alpha}. \quad (3)$$

4 Projection defocus based on multi-scale kernels

4.1 Deblur kernel model estimation

The defocus image, which is a type of degraded image based on the original projection image, can be described as a visual blur artifact and is affected by several disturbance factors. In recent studies, most researchers have used classical image restoration methods to solve the projection defocus problem. Analyzed at the per-pixel level, the projector system throws one pixel from the electronic imaging space to an out-of-focus blur area on the display surface, which is processed by some linear or nonlinear blur functions. Considered at the whole-image level, the blur effect can be described as the convolution computed by blur kernels (Fig. 1) (Zhang and Nayar, 2006). Therefore, the essence of solving the defocus problem lies in finding the deblur kernel or defocus kernel to construct the defocus function model.

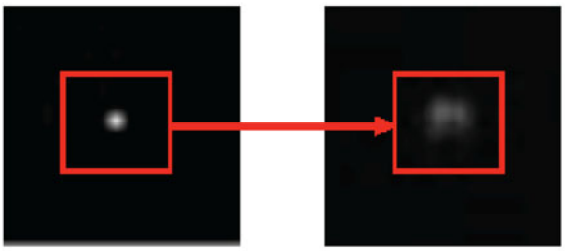

Fig. 1 Projection blur image
The original feature in the colored frame of (a) is projected on the display surface, and (b) is the corresponding blurred feature

In ideal cases, the projection blur model can be parameterized to the common convolution equation as follows (I_{orig} is the original projection image, and $\circ$ is convolution computation):

$$I_{blur} = I_{orig}\circ h_\sigma. \quad (4)$$

According to the projection imaging theory of the DLP projector and from experiments on linear and nonlinear parameterization display surfaces for popular DLP projectors, the projection blur model can be

simplified to the unique Gaussian filter kernel, h, which can be applied to the entire projection image for deconvolution:

$$h_\sigma(x,y)=\frac{1}{2\pi\sigma^2}\exp\left(-\frac{x^2+y^2}{2\sigma^2}\right). \quad (5)$$

According to Eq. (1) and analysis of deconvolution computation, the estimated blur kernel can be used to construct the projection deblur function, F_{defocus} (Eq. (6)). If F_{defocus} is applied to the original image in the projector imaging space, the observer can see the projection image more clearly and sharply in the projection display environment.

$$I_{\text{defocus}}=F_{\text{defocus}}(I_{\text{orig}}). \quad (6)$$

4.2 Improved focus evaluation function

First, as Fig. 2a shows, the original feature image is equally divided into separated sub-image areas (the 'sub-image area' means the image pixels within each white rectangle frame as indicated). Here, the 25×25 dense 'dot' feature patterns are applied as centers of each sub-image area and the size of one sub-image area is 21×21 pixels. Then these sub-images are regrouped and indexed as an original feature sub-image cluster. Second, the captured projection image (Fig. 2b) is processed by applying the feature recognition algorithm (as in the method in Section 3.1) to obtain the exact coordination position of each 'dot' feature pattern; according to the pixel corresponding mapping between the projector and the camera from Section 3.1, we can finally obtain the corresponding sub-image cluster in the captured projection image. To analyze the computation data, an improved focus evaluation algorithm is applied that estimates the sharpness of each sub-image area.

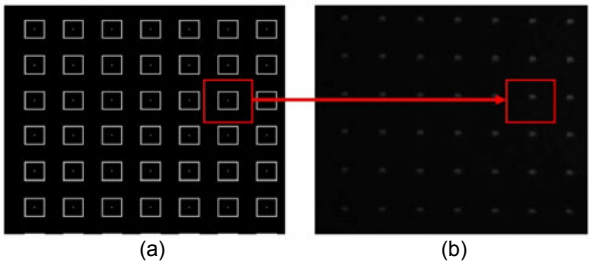

Fig. 2 Recognition and computation of corresponding sub-image clusters

(a) Original encoded feature pattern image; (b) Captured encoded feature pattern image

At present, popular focus evaluation methods include the gray-scale difference method, Laplacian operator method, and Sobel-Tenengrad (ST) method. According to these experiments, the first two methods are more efficient than the third one, but the ST method has the best accuracy and robustness. So, for the projection defocus problem, the ST method is used, but with some improvements to increase its speed.

The basic simple Sobel operator is the 3×3 kernel format, but considering the throw ratio of popular projectors, 5×5 (Fig. 3) and 7×7 extended Sobel operators must be constructed to analyze sub-image clusters in the spatial domain.

2	3	0	-3	-2
3	4	0	-4	-3
6	6	0	-6	-6
3	4	0	-4	-3
2	3	0	-3	-2

(a)

2	3	6	3	2
3	4	6	4	3
0	0	0	0	0
-3	-4	-6	-4	-3
-2	-3	-6	-3	-2

(b)

Fig. 3 The 5×5 *X*-direction (a) and *Y*-direction (b) Sobel operator

First, the gradient value of every pixel in each sub-image is computed using the extended Sobel operator. Then, T_x and T_y are set, indicating the results in the horizontal and vertical directions, respectively. In the spatial domain of the sub-image, the computation of T_x and T_y can be expressed as a convolution filter computation with the Sobel operator:

$$T_x=I_{\text{sub}}(x,y)\circ S_x, \quad (7)$$

$$T_y=I_{\text{sub}}(x,y)\circ S_y. \quad (8)$$

Second, the classical Tenengrad focus evaluation function is improved to compute the degree of sharpness of the sub-image cluster. As Eq. (9) shows, the classical Tenengrad function requires a large amount of computation, so it has the highest evaluation accuracy but is less efficient. In most practical calculations, Eq. (9) can be transformed to an approximate format given as Eq. (10).

$$F_{\text{ST}}=\sum_{x=0}^{M-1}\sum_{y=0}^{N-1}\sqrt{T_x^2+T_y^2}, \quad (9)$$

$$F_{\text{ST-abs}}=\sum_{x=0}^{M-1}\sum_{y=0}^{N-1}\left(|T_x|+|T_y|\right). \quad (10)$$

Experimentally, the evaluation result of Eq. (9) is equivalent to that of Eq. (10). To analyze the results in the X and Y directions, in our study Eq. (10) is divided into separate parts and reconstructed as two new evaluation functions:

$$F_{\text{ST-}x}=\sum_{x=0}^{M-1}\sum_{y=0}^{N-1}|T_x|, \tag{11}$$

$$F_{\text{ST-}y}=\sum_{x=0}^{M-1}\sum_{y=0}^{N-1}|T_y|. \tag{12}$$

Then, compared to the classical ST function, the captured projection feature image is set to be the sample data, and the evaluation results of the new X/Y-direction ST functions have very similar curves (Fig. 4). In other words, we can obtain very similar indices of the peak values from these three Tenengrad focus evaluation functions. According to previous analysis, the X/Y-direction ST focus function yields a very similar sharpness evaluation value but is much faster. In the experiments, the new evaluation function takes only 1/15 to 1/20 of the computational time of the original function.

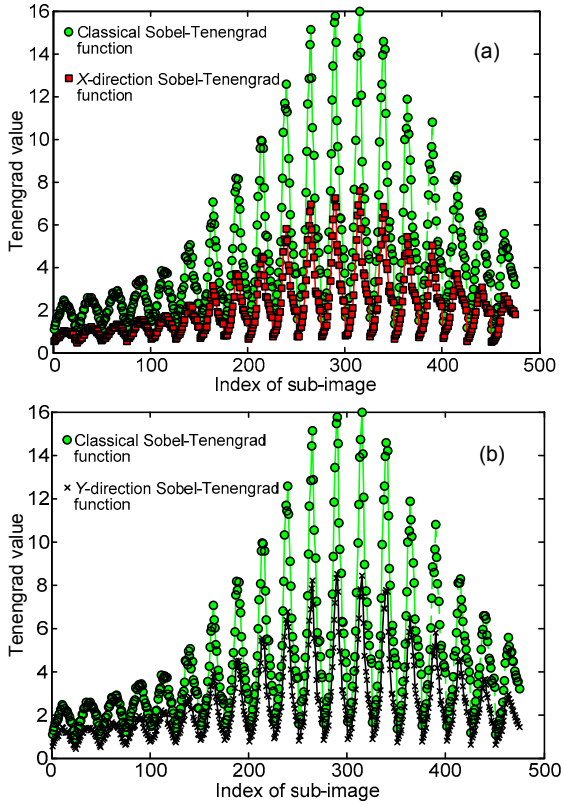

Fig. 4 Analysis of the improved Sobel-Tenengrad evaluation function

(a) Classical Sobel-Tenengrad function vs. X-direction Sobel-Tenengrad function; (b) Classical Sobel-Tenengrad function vs. Y-direction Sobel-Tenengrad function

As shown in Fig. 5, the improved ST function is used to compute each mapping pixel area of the original feature sub-image (Fig. 2). The area with the highest sharpness is then assigned as the defocus reference template, I_{ref}.

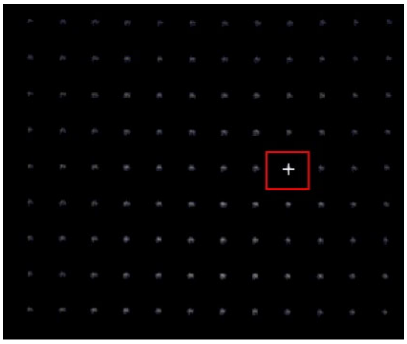

Fig. 5 Recognized 'dot' feature of defocus reference template I_{ref}, indicated by a white cross within the rectangle frame

4.3 Luminance equalization

Because of the hardware limitation of the projector imaging system, the projection pixels in the center area have higher lumen values than those at the boundaries. Such nonuniform projection lumens spread the effects of defocus function computation. Based on the improved ST focus evaluation function from Section 4.2, a luminance equalization method is proposed to preprocess the captured projection images and optimize the defocus algorithm using the following procedure:

Step 1: The focus reference template is transformed by applying a fast Fourier transform (FFT):

$$I_{\text{FFT-ref}}=\text{FFT}(I_{\text{ref}}). \tag{13}$$

Step 2: According to the mathematical theory of FFT, the direct current portion of the image equals the intensity value at the original position, and when the original captured projection image is transformed from the spatial domain to the frequency domain, the frequency spectrum information in the direct current part does not change. For a more detailed explanation, see the Gaussian filter function (Eq. (14)). When u and v equal zero, the location is at the original position, and

$F(0, 0)$ equals the average intensity value of the original image (Eq. (15)). Then the intensity value, $I_{\text{FFT-ref}}(0, 0)$, as the direct current part of $I_{\text{FFT-ref}}$, is extracted and saved for the following computation (Eq. (16)).

$$F(u,v)=\frac{1}{MN}\sum_{x=0}^{M-1}\sum_{y=0}^{N-1}f(x,y)\exp\left(-\mathrm{j}2\pi\left(\frac{ux}{M}+\frac{vy}{N}\right)\right), \tag{14}$$

$$F(0,0)=\frac{1}{MN}\sum_{x=0}^{M-1}\sum_{y=0}^{N-1}f(x,y), \tag{15}$$

$$I_{\text{FFT-ref}}(0,0)=\frac{1}{MN}\sum_{x=0}^{M-1}\sum_{y=0}^{N-1}I_{\text{ref}}(x,y). \tag{16}$$

Step 3: The FFT computation is applied over each image area, I_n, in the sub-image cluster, and the frequency sub-image cluster, $I_{\text{FFT-}n}$, is obtained. In the frequency domain, all the original position intensity values $I_{\text{FFT-}n}(0, 0)$ are replaced by $I_{\text{FFT-ref}}(0, 0)$ from step 2, and then an inverse Fourier transform is applied to each of them, returning to the spatial domain:

$$I_n'=\text{invFFT}(I_{\text{FFT-}n}). \tag{17}$$

The new sub-image cluster in the spatial domain is I_n', which is then reconstructed as the per-pixel correspondence mapping from Section 3.1. The final remapped image can then be rendered as a luminance-equalized projection image (Fig. 6).

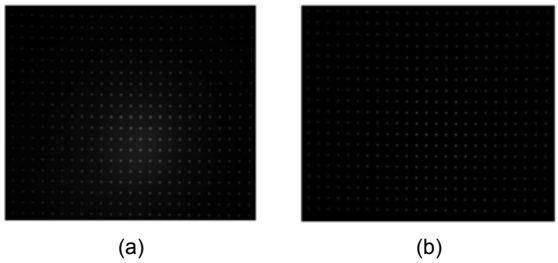

Fig. 6 Luminance equalization
(a) Original captured image; (b) Luminance-equalized captured image

4.4 Multi-scale Gaussian convolution kernel template estimation

First, the focus reference image I_{ref} is set as the basis of the convolution reference template, and the multi-scale Gaussian filter convolution is applied to process it. In the Gaussian filter convolution Eq. (2), the sigma value is adjusted to equal 0.5, 1, 1.5, 2, 2.5, 3, 3.5, and 4, so the convolution computation produces eight different Gaussian filter images, which can then be set as multi-scale Gaussian convolution kernel templates (Fig. 7).

Then the sharpness degree of each convolution kernel template is computed based on the improved ST focus evaluation function. The same method is applied to every sub-image area and the results compared to the kernel templates. The sharpness degree best matched with the sub-image area is chosen and assigned the same index used for the sub-image cluster.

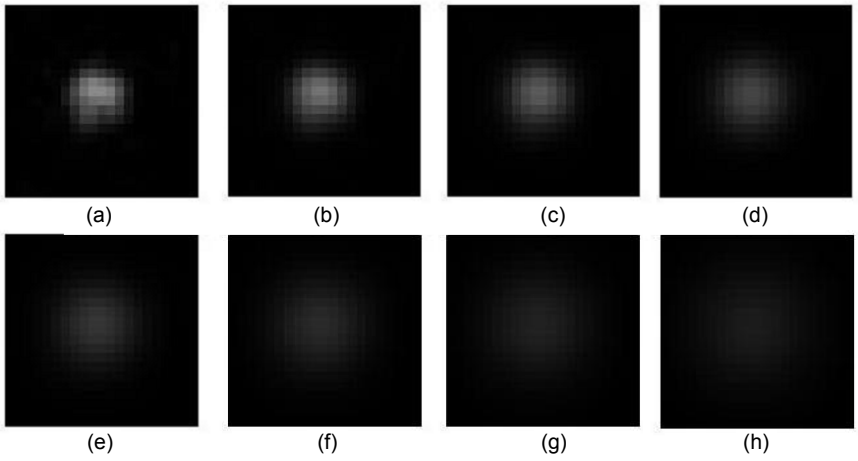

Fig. 7 Multi-scale Gaussian convolution kernel templates: (a) sigma=0.5; (b) sigma=1; **(c) sigma=1.5**; **(d) sigma=2**; **(e) sigma=2.5**; **(f) sigma=3; (g) sigma=3.5; (h) sigma=4**

Finally, the sub-image cluster is defocused and regrouped. Then, the classical Wiener filter function is chosen as in the deconvolution method and Eq. (18) is applied to transform the original projection image to the frequency domain.

$$I_{\text{freq}}(u,v) = I(u,v) \cdot H(u,v), \tag{18}$$

$$I_{\text{Wiener}} = \frac{H'(u,v) \cdot I_{\text{freq}}(u,v)}{\left| H(u,v)^2 + 1/\text{SNR} \right|}. \tag{19}$$

In Eq. (18), the Gaussian filter kernel is set as $H(u, v)$, and the sigma value is replaced by the previous eight groups of estimation values. The SNR in Eq. (19) means the signal-to-noise ratio.

For regrouping and rendering a defocus projection image, a multi-scale defocus image template method is proposed. Some previous regrouping methods choose the corresponding sigma value of each sub-image to do a separate deconvolution, and then regroup and index the deconvolved sub-images. However, when the feature patterns are large (more than 1000), these methods devote much time to discrete computations and repeat graphics rendering for each sub-image area. For this study, the previous regrouping method is simplified and improved to work with real-time computational resources. First, a deconvolution computation using the Wiener filter method with eight groups of estimated sigma values is applied to the entire original projection image. After deconvolution computation, eight whole Wiener filter images are obtained (Fig. 8) and saved as remapping defocus image templates in the frame buffer of the graphics card. Then, each pixel is traversed repeatedly for each sub-image area of the original projection image, replacing the pixel value by the same position in the corresponding defocus image templates. For optimization to boundary rendering, the bilinear interpolation-rendering algorithm is applied to smooth the computation of the boundary pixels. The final regrouped and rendered new image is the 'projection defocus compensation image' (Fig. 9).

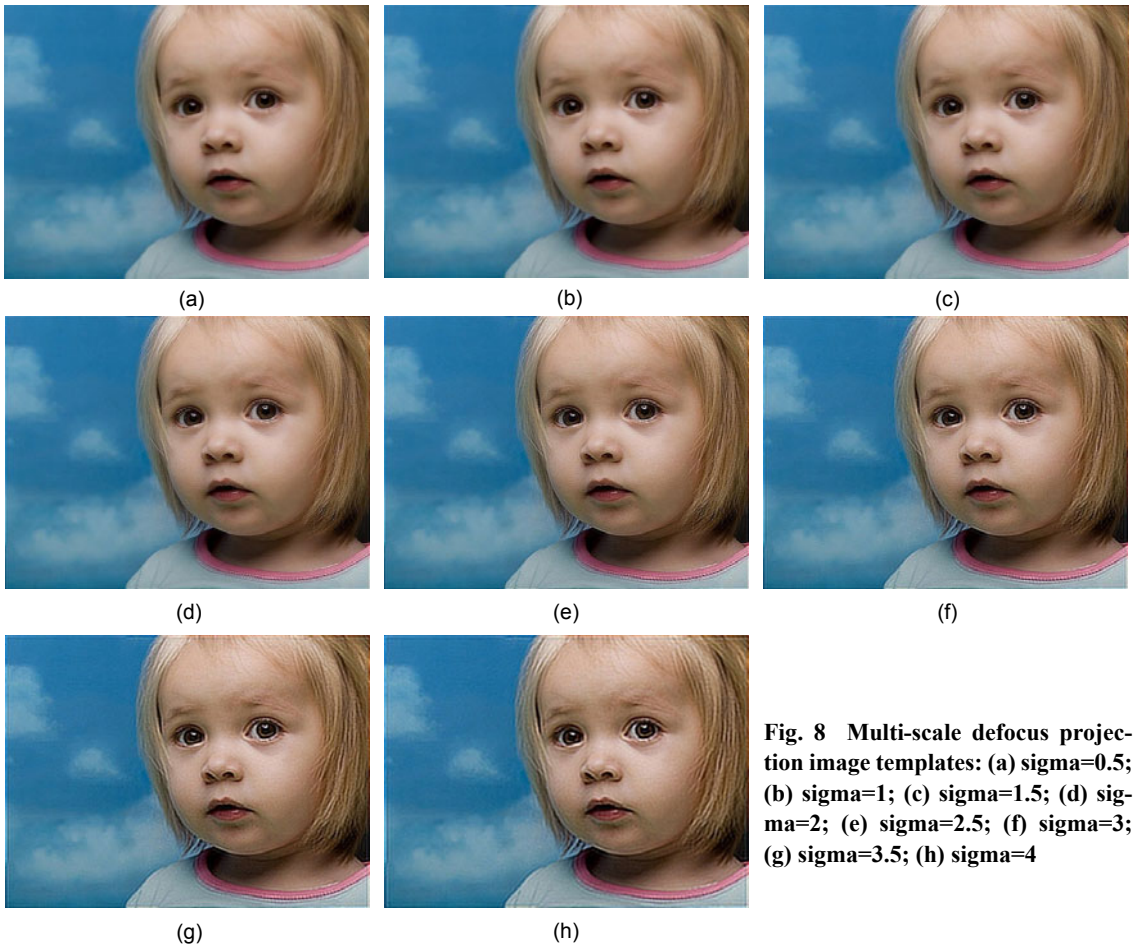

Fig. 8 Multi-scale defocus projection image templates: (a) sigma=0.5; (b) sigma=1; (c) sigma=1.5; (d) sigma=2; (e) sigma=2.5; (f) sigma=3; (g) sigma=3.5; (h) sigma=4

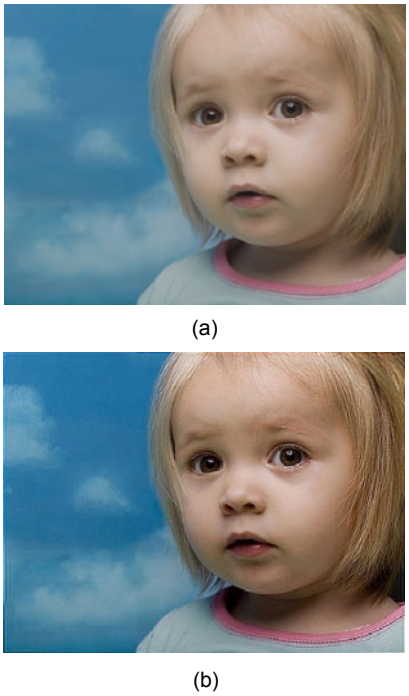

Fig. 9 Projection defocus compensation image computation
(a) Original projection image; (b) Projection defocus compensation image

5 Experiments and analysis

Fig. 10 shows a smart adaptive defocus projection system designed and implemented for this study (Zhu *et al*., 2011a; 2011b). The system prototype consists of a Lenovo T151 DLP projector and a Logitech C905 camera for projection and capture, and uses a biaxial digital tilt sensor attached to the side of the projector to feed back the real-time projection positions. All the programs are running on a laptop, which is connected to all the instruments. The key calibration and communication algorithms are coded using Matlab and C++, and the graphics texture mapping is rendered using OpenGL libraries.

The main algorithm flow chart of this work is shown in Fig. 11. First, the projection system is initialized and geometrically calibrated using a discrete mapping algorithm. Then, a radiometric compensation method based on an improved Lambertian reflection model is used to eliminate the color texture and environmental radiometric disturbance. Second, the improved ST focus evaluation function is proposed to calculate the sharpness degree and equalize the projection luminance. Based on sharpness degree computation, the multi-scale defocus estimation kernels are constructed to render multi-scale defocus projection images, which are then used to remap and render the projection defocus compensated images. The final produced projection images are projected directly from the computer graphics texture mapping space.

Fig. 10 Prototype of the intelligent projection system

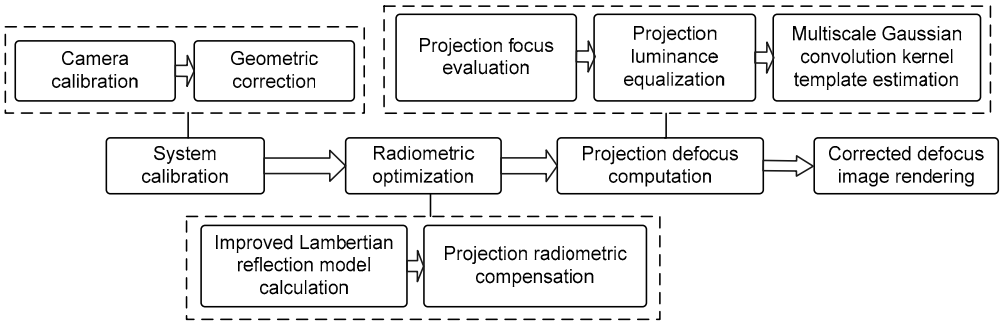

Fig. 11 Flow chart of the projection defocus compensation algorithm, which has four key procedures: system calibration, radiometric optimization, projection defocus computation, and corrected defocus image rendering

For the experiments, the projection display environment is a planar vertical wall in an office room, and the projected surface is perpendicular to the axis of projection. The position of the 'hardware focused' projector is then adjusted to simulate the 'projection defocus effect'. The projected test images are chosen with resolution of 1024×768, the same as the maximum projection resolution of the projector used in this study.

In Experiment 1, when the original projection image is projected directly on the surface (Fig. 12a), the blurred image and color cast vision artifacts are obvious. After the proposed defocus algorithm is applied (Fig. 12b), the perception resolution of the projection image is much enhanced.

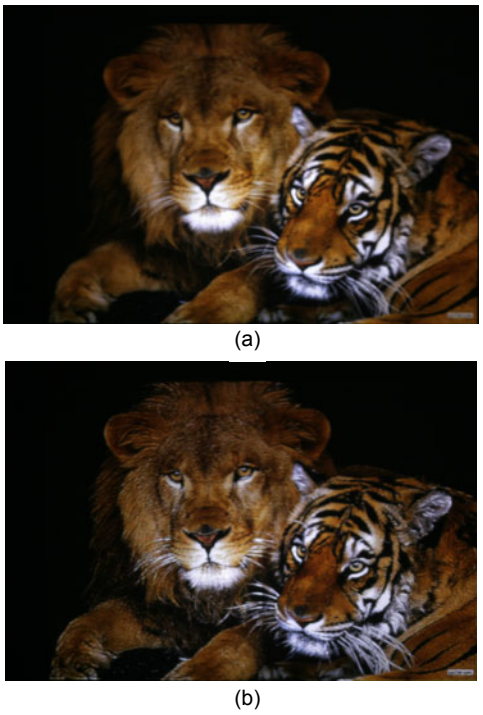

(a)

(b)

Fig. 12 Results of Experiment 1

In local area analyses about corrected projection image (b), details of the hair of the lion and the beard of the tiger can be observed, and the sharpness and color of the whole picture are similar to those of the original image (a)

As Fig. 13 shows, the same defocus effects can be observed in Experiment 2.

To evaluate the defocus improvement of the algorithm, we obtain the defocus evaluation results for Experiment 2. The improvement of the projection image defocus effect is a sort of subjective visual perception of the human observer, so it is difficult to adapt a common calculation criterion for projection defocus algorithms. To evaluate the algorithm described here, we apply both subjective and objective methods.

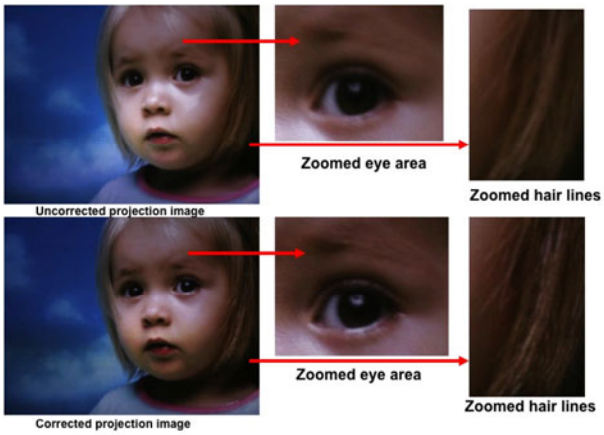

Fig. 13 Results of Experiment 2

The magnification of various regions of the captured experimental images shows that the detailed textures in the eye and hair regions (top row) of the image are difficult to distinguish. From the captured defocused projection image, an observer can detect clear textures in the eyebrows and eyelashes, and the hair shows many more smooth lines (bottom row)

For subjective assessment, the Double Stimulus Continuous Quality Scale (DSCQS) method set in ITU-R BT.500 is applied. The DSCQS method, which is particularly effective when it is not possible to present the full range of quality conditions, has been widely used for assessing the video quality of television broadcasts. It can simultaneously assess the difference in quality between a reference video and an assessment video (ITU, 2002). We invite 10 people of different knowledge backgrounds as observers to judge the visual perception of the defocus effect. A pair of videos comprising the uncorrected projection image sequence and the defocus projection image sequence is projected twice on the display surface. The observers are not told which is the defocus corrected projection. As Fig. 14 shows, the assessments of the observers are recorded the second time the videos (Videos C and D) are presented (NTT, 1999).

The assessment score system is based on categories of the five-grade quality scale: Excellent, Good, Fair, Poor, Bad. The evaluations are normalized to the score range 0–100 (Bad, 0; Excellent, 100). By

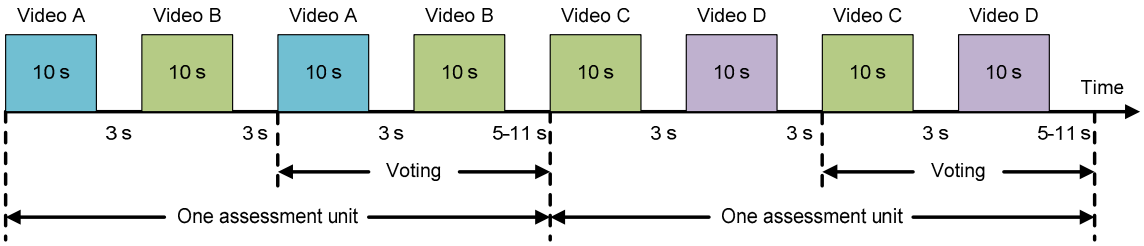

Fig. 14 Schematic of the Double Stimulus Continuous Quality Scale (DSCQS) method
Videos A and D: uncorrected projection image sequence; Videos B and C: defocus corrected projection image sequence

calculating the scores from observers for separated image sequence videos, we obtain an average assessment of uncorrected defocus projection and of corrected defocus projection (Table 1).

Table 1 Assessment scores given by 10 observes using the DSCQS method

Observer ID	Quality grade	
	Uncorrected projection Video D	Defocus corrected projection Video C
1	Poor	Good
2	Poor	Fair
3	Bad	Good
4	Poor	Good
5	Fair	Excellent
6	Poor	Good
7	Poor	Good
8	Bad	Fair
9	Poor	Good
10	Fair	Good
Average improvement	25.0	72.5

The average score of uncorrected projection is 25.0 and that of defocus corrected projection is 72.5, which shows a remarkable improvement from Poor to almost Good grade visual perception.

For an objective evaluation of defocus projection quality, we choose the classical image blur evaluation method to compute the blur degree of the uncorrected projection image and of the defocus projection image, and then calculate the difference between them. We name the original projection image 'error-Focus I' and the corrected one 'error-Focus II'.

Table 2 shows that, using the algorithm proposed here we can obtain 8% defocus improvement for the whole image area. More than that, for interesting and more detailed areas, there is an 8.02% improvement at the hair location and a 16.94% improvement at the eye location, confirming significant defocus accuracy. In contrast, in Brown *et al*. (2006) and Ladha *et al*. (2011), who used a similar single camera-projector defocus system, only a defocus effect of less than 13% can be obtained. These results show that our defocus algorithm achieves better defocus correction. With respect to algorithm efficiency, the computational time for system calibration is approximately 5–10 s, and the defocus correction for one frame costs approximately 0.1–0.2 s, which satisfies everyday needs for a presentation display speed.

Table 2 Defocus projection improvement of Experiment 2

Area	Error-Focus I (pixel)	Error-Focus II (pixel)	Improvement
Whole image	0.8289	0.7626	8.00%
Hair	6.3185	5.8118	8.02%
Eye	1.6819	1.3971	16.94%

According to the accuracy and efficiency achieved by our projection defocus algorithm, the defocus effects and sharpness improvement satisfy an observer's visual observation criterion almost in real time.

6 Conclusions and future research

We propose a defocus algorithm to deal with projection images based on multi-scale convolution kernel templates. The algorithm runs on a self-designed smart projection system. Based on geometric calibration and radiometric compensation optimization for projection images, the main projection defocus correction algorithm applies a novel modified ST focus evaluation function to calculate the degree of sharpness for intensity equalization, and constructs multi-scale defocus convolution kernels to remap and render the defocus projection images. The final projection defocus compensated images can eliminate out-of-focus defects and improve the sharpness of

uncorrected images. Experiments show that the resolution and clarity of the observer's visual perception are significantly improved.

There are still some problems to be considered. The current algorithm takes approximately 0.1–0.2 s for one frame, satisfying the requirements for common real-time presentation displays. For super-high-resolution video play, however, the frame rate must be increased to 24 frames/s or higher. Future research work will focus primarily on speeding up the algorithm while retaining high correction accuracy. Hopefully, significant progress can be made by researching hardware acceleration technology, such as a GPU computing method based on CUDA architecture.

References

Ashdown, M., Okabe, T., Sato, I., Sato, Y., 2006. Robust Content-Dependent Photometric Projector Compensation. Proc. Conf. on Computer Vision and Pattern Recognition Workshop. [doi:10.1109/CVPRW.2006.172]

Bhasker, E., Juang, R., Majumder, A., 2007. Registration techniques for using imperfect and partially calibrated devices in planar multi-projector displays. *IEEE Trans. Visual. Comput. Graph.*, **13**(6):1368-1375. [doi:10.1109/TVCG.2007.70586]

Bimber, O., Emmerling, A., 2006. Multifocal projection: a multiprojector technique for increasing focal depth. *IEEE Trans. Visual. Comput. Graph.*, **12**(4):658-667. [doi:10.1109/TVCG.2006.75]

Bimber, O., Iwai, D., Wetzstein, G., Grundhöfer, A., 2008. The visual computing of projector-camera systems. *Comput. Graph. Forum*, **27**(8):2219-2245. [doi:10.1111/j.1467-8659.2008.01175.x]

Brown, M., Majumder, A., Yang, R.G., 2005. Camera-based calibration techniques for seamless multiprojector displays. *IEEE Trans. Visual. Comput. Graph.*, **11**(2):193-206. [doi:10.1109/TVCG.2005.27]

Brown, M.S., Song, P., Cham, T.J., 2006. Image Preconditioning for Out-of-Focus Projector Blur. Proc. IEEE Computer Society Conf. on Computer Vision and Pattern Recognition, p.1956-1963. [doi:10.1109/CVPR.2006.145]

Grossberg, M.D., Peri, H., Nayar, S.K., Belhumeur, P.N., 2004. Making One Object Look Like Another: Controlling Appearance Using a Projector-Camera System. Proc. IEEE Conf. on Computer Vision and Pattern Recognition, **1**:452-459. [doi:10.1109/CVPR.2004.1315067]

Grosse, M., Wetzstein, G., Grundhöfer, A., Bimber, O., 2010. Coded aperture projection. *ACM Trans. Graph.*, **29**(3), Article 22, p.1-12. [doi:10.1145/1805964.1805966]

ITU, 2002. Methodology for the Subjective Assessment of the Quality of Television Pictures. ITU Recommendation BT 500-11. International Telecommunication Union.

Ladha, S., Smith-Miles, K., Chandran, S., 2011. Projection Defocus Correction Using Adaptive Kernel Sampling and Geometric Correction in Dual-Planar Environments. IEEE Computer Society Conf. on Computer Vision and Pattern Recognition Workshops, p.9-14. [doi:10.1109/CVPRW.2011.5981686]

Nagase, M., Iwai, D., Sato, K., 2011. Dynamic defocus and occlusion compensation of projected imagery by model-based optimal projector selection in multi-projection environment. *Virtual. Real.*, **15**(2-3):119-132. [doi:10.1007/s10055-010-0168-4]

Nayar, S.K., Peri, H., Grossberg, M.D., Belhumeur, P.N., 2003. A Projection System with Radiometric Compensation for Screen Imperfections. Proc. ICCV Workshop on Projector-Camera Systems, p.1-8.

NTT, 1999. Video Quality Assessment Methods: 1.5.(5). Citing Electronic Sources of Information. Network Technology Laboratories. Available from http://www.ntt.co.jp/qos/qoe/eng/technology/visual/01_5_5.html.

Oyamada, Y., Saito, H., 2009. Blind Deconvolution Based Projector Defocus Removing with Uncalibrated Projector-Camera Pair. IEEE Int. Workshop on Projector-Camera Systems.

Raskar, R., Welch, G., Cutts, M., Lake, A., Stesin, L., Fuchs, H., 1998. The Office of the Future: a Unified Approach to Image-Based Modeling and Spatially Immersive Displays. Proc. 25th Annual Conf. on Computer Graphics and Interactive Techniques, p.179-188. [doi:10.1145/280814.280861]

Wang, X.H., Hua, W., Bao, H.J., 2007. Global color correction for multi-projector tiled display wall. *J. Comput.-Aided Des. Comput. Graph.*, **19**(1):96-101 (in Chinese).

Xie, L.J., Zheng, Y., Yang, T.J., Gao, W.X., Pan, N.H., 2007. SimWall: a practical user-friendly stereo tiled display wall system. *J. Zhejiang Univ.-Sci. A*, **8**(4):596-604. [doi:10.1631/jzus.2007.A0596]

Yang, T.J., Xie, L.J., Zheng, Y., Gao, W.X., Pan, N.H., 2007. Construction of a large scale stereo display wall system. *J. Comput.-Aided Des. Comput. Graph.*, **19**(8):953-959 (in Chinese).

Zhang, L., Nayar, S., 2006. Projection defocus analysis for scene capture and image display. *ACM Trans. Graph.*, **25**(3):907-915. [doi:10.1145/1141911.1141974]

Zhang, Z.Y., 2000. A flexible new technique for camera calibration. *IEEE Trans. Pattern Anal. Mach. Intell.*, **22**(11):1330-1334. [doi:10.1109/34.888718]

Zhu, B., Xie, L.J., Wang, Q.H., Yang, T.J., Zheng, Y., 2011a. An Intelligent Projection System Adapted to Arbitrary Surfaces. First Int. Conf. on Instrumentation, Measurement, Computer, Communication and Control, p.293-298. [doi:10.1109/IMCCC.2011.80]

Zhu, B., Xie, L.J., Yang, T.J., Wang, Q.H., Zheng, Y., 2011b. A novel radiometric projector compensation algorithm based on Lambertian reflection model. *SPIE*, **8004:** 80040I-1-80040I-5. [doi:10.1117/12.901092]

Zhu, B., Xie, L.J., Yang, T.J., Wang, Q.H., Zheng, Y., 2012. An adaptive calibration algorithm for projected images in everyday environment. *J. Comput.-Aided Des. Comput. Graph.*, **24**(7):941-948 (in Chinese).